

Stability of Fe₂S and Fe₁₂S₇ to 125 GPa; implications for S-rich planetary cores

C.C. Zurkowski, B. Lavina, S. Chariton, V. Prakapenka, A.J. Campbell

Supplementary Information

The Supplementary Information includes:

- Experimental Methods
- Structural Relationship of the Fe₂S Polymorphs and Fe₁₂S₇
- Tables S-1 and S-2
- Figures S-1 to S-3
- Appendices A-1 to A-4
- Supplementary Information References

Experimental Methods

The high pressure and temperature conditions for iron sulfide synthesis were achieved in a laser-heated diamond anvil cell (DAC). The starting material used in this study consisted of Fe (>99.9 %, <10 μm, Alfa Aesar) powder and iron sulfide (FeS, 99.99 %, Alfa Aesar) mixed into a ratio of 1g Fe to 1.78 g FeS (referred herein to as Fe₆₆S₄₄). The starting material was homogenised in a pestle and mortar for one hour in alcohol, dried, and then mixed dry for a short time. This final dry mixing accounts for density separation during alcohol evaporation and is conducted for a short duration to limit Fe-oxidation. The material was then compressed into foils between two ungasketed diamond anvils prior to loading.

Pressure was generated using short symmetric and BX-90-type diamond anvil cells equipped with Bohler-Almax conical diamonds and seats. Diamonds with 150 μm culets that beveled to 300 μm were used. Sixty-micron sample chambers drilled out of preindented rhenium gaskets were each loaded with a sample foil placed between layers of KCl pressure transmitting medium. The loaded samples were finally baked at 120 °C for 30 minutes prior to pressurisation. During compression, the equation of state of KCl (Dewaele *et al.*, 2012) was used to monitor pressure. The agreement between measured unit-cell parameters and structural refinement models for multiple grains of each phase in this study, support that deviatoric strain from the quenched KCl medium did not play a major role in the observed structural geometries and did not inhibit structural analysis.

Double sided laser heating of the pressurised samples was conducted at beamline 13-ID-D (GeoSoilEnviroCARS) of the Advanced Photon Source, Argonne National Laboratory. The lasers were aligned to the X-ray beam using the fluorescence of the KCl insulator (Prakapenka *et al.*, 2008). Lasers shaped with ~ 15 μm flat tops were used and temperature was measured spectroradiometrically based on the thermal emission from the central 6 μm diameter of the laser heated spot (Heinz and Jeanloz, 1987). To account for temperature gradients within the sample chamber, a 3 % correction was applied based on Campbell *et al.*, (2007, 2009). The samples were heated in ~ 30 minute cycles in the 105–125 GPa pressure range. Each sample location was heated once. Two heating experiments were carried out in this study. Run 1 was conducted on the $\text{Fe}_{66}\text{S}_{34}$ starting composition at 105.3 (9) GPa (values in parentheses are propagated uncertainties on the last reported digits) and quenched from 2400 (120) K. The sample was then pressurised to 125 (1) GPa and heated to 2260 (140) K prior to quenching in Run 2. A summarisation of the experimental conditions and instrument parameters used in this study is given in Table S-1.

Upon quenching at each pressure, X-ray diffraction was conducted at beamlines 13-ID-D (GeoSoilEnviroCARS) of the Advanced Photon Source, Argonne National Laboratory. Diffraction measurements were collected with a 2 μm by 3 μm full width at half maximum (FWHM) incident X-ray beam at 42 keV on a CdTe 1M Pilatus detector (Table 1). Around the centre of the laser heated spots, 10×10 μm diffraction maps were collected in 3 μm steps to assess the regions of optimal grain growth. Centred at selected map locations, the sample was rotated across a $\pm 30^\circ$ angular range, as diffraction images were collected in 0.5° steps. X-ray exposure time of 2–4 s were used during the rotational step scans. Due to the small size of the sample chambers, ~ 30 μm at target pressures, diffraction from the rhenium gasket was also observed in the rotational scans.

Grains of Fe_2S and Fe_{12}S_7 were identified in the reciprocal space and the reflections from each grain were isolated from reflections associated with other sulfide grains, iron, rhenium, KCl, and diamond. The target phases were indexed in the reciprocal space and the intensities of the reflections were integrated across the rotational scan using CrysAlis Pro (Rigaku Oxford Diffraction, 2018). The unit-cell parameters and structure factors were then implemented into the SHELXT structure solution program (Sheldrick, 2015a) and the atomic coordinates and displacement parameters were refined for each structure using SHELXL2014/7 (Sheldrick, 2014, 2015b). Raw diffraction images were examined and integrated using Dioptas (Prescher and Prakapenka, 2015) and VESTA was used for structure model visualisation and graphical renderings of the iron sulfides examined in this study.

Several components of high P - T synthesis do limit the capability to structurally solve and refine these crystal structures; namely, limited angular sample access in the diamond-anvil cell, overlap in diffraction angles of target phases with diffraction from other grains; rhenium; and the KCl insulator, and the volume of the grain illuminated by the X-ray beam. Despite these challenges, sufficient reflections were obtained to structurally solve and refine structure models for the Fe-sulfide phases observed in this study (Table S-2). For the refinement models shown in Table S-2, an independent-reflection-to-parameter ratio greater than 6 was maintained, a value typically suggesting that a sufficient number of reflections were collected for the number of refined parameters in the structure models at these high-pressure conditions (*e.g.*, Lavina *et al.*, 2014). The structures were refined with anisotropic displacement parameters on the metal atoms if enough reflections were collected and a significant improvement to the refinement model was observed. Alternatively, in the case of limited reflections or when adding anisotropic displacement to the metal sites did not result in a significant



change in the model quality, all sites were refined with isotropic displacement parameters. The errors on metal site occupancies are provided in Table S-2 for each refinement model and support the reported stoichiometries for the Fe-sulfides analysed. CIF files for the refined structures (Table S-2) are provided in the appendices of this work.

Structural relationship of the Fe₂S polymorphs and Fe₁₂S₇

Two high *P-T* experiments were conducted: Runs 1 and 2 were performed at 105.3 (9) GPa and quenched from 2400 (120) K and 125 (1) GPa and quenched from 2260 (140) K, respectively (Table S-2). After each heating, rotational diffraction scans were collected at various locations around the heated region to assess the phase relations. At the centre of the laser heated spot, hexagonal Fe₂S and Fe₁₂S₇ were synthesised (Fig. 1); however, grains of C23 Fe₂S (Co₂P-type, *Pnma*, *Z* = 4). and Fe₁₂S₇ were identified in the lower temperature regions of the laser heated spot (Fig. S-1, Table 1) (Zurkowski *et al.*, 2022). In Run 2, similar results were obtained (Table S-2), and additionally, a body-centred orthorhombic lattice with parameters *a* = 5.382 (1) Å, *b* = 6.103 (4) Å, *c* = 9.098 (4) Å (Fig. S-1, Table S-2) was synthesised. The volume of this lattice is compatible with 12 formula units of Fe₂S. Grains of C23 Fe₂S were also identified within the laser-heated region (Table 2).

Our crystal-chemical analyses across the laser heated spot after each heating cycle, suggests that the Co₂P-type, C23 Fe₂S is a low-temperature polymorph while the Fe₂P-type, C22 Fe₂S is a high-temperature polymorph. Agreeably, previous studies have observed the C23 structure as a lower temperature *M₂X* polymorph of C22 *M₂X* phases (Ellner and Mittemeijer, 2001). While the *P-T* conditions in Runs 1 and 2 suggest that temperatures within the laser-heated region cross the C23–C22 thermal boundary, the diffraction patterns collected after Run 2 mainly consist of a larger, body-centred orthorhombic Fe₂S lattice (Table S-2, Fig. S-1). The observed reflections of the unknown phase constrain an *Imm2* space group, and structure was solved and refined to a Cr₂P-type Fe₂S (Table 2; Figs. 2c, S-2; Appendix A-3) (Artigas *et al.*, 1996). This structure can be viewed as a slight shifting of the polyhedra in the C22 and C23 structures with polyhedral symmetry that is transitional between the C23 and C22 structures (Figs. S-2, S-3). The Cr₂P-type structure has previously been reported as a low temperature modification of the C22 structure (Artigas *et al.*, 1996). In the Fe-S system, however, observations of the Cr₂P-type Fe₂S near the C23–C22 *P-T* boundary, suggests that Cr₂P-type Fe₂S is a transitional phase forming as the polyhedra of the C23 structure shift into the C22 structure. The deviation from full occupancy for the Fe and S sites refined in the Cr₂P-type Fe₂S structure models (Table 2) are larger than that observed for the other phases examined in this study, suggesting that the Cr₂P-type Fe₂S grains were not well formed and may be metastable. Furthermore, diffraction observed from this phase shows clustering of small grains supporting that the single crystals are not well formed (Fig. S-1). The possibilities that Cr₂P-type Fe₂S is an equilibrium phase or a distortion that formed on quench cannot be ruled out and require further experiments.

Fe₁₂S₇ is observed in all heating cycles to adopt a hexagonal structure with a *P-6* space group. The structure was solved and refined to the Co₁₂P₇ structure (*Z* = 1) (Zurkowski *et al.*, 2022) (Figs. 1, S-2, Appendix A-2). All sites are fully occupied within an error of 6 %, ruling out the Cr₁₂P₇ structure (Chun and Carpenter, 1987). The Co₁₂P₇ structure is closely related to the C22, C23 and Cr₂P-type Fe₂S structures, in that it is composed of columns of edge sharing FeS₅ square pyramids (green) and columns of corner sharing



FeS₄ tetrahedra (blue) linked along edges along the *c* direction. Fe₁₂S₇ has an increased ratio of square pyramid to tetrahedral building blocks compared to the Fe₂S polymorphs, resulting in the formation of trigonal channels along the *c* direction (Figs. S-2, S-3). The interatomic distances in Fe₁₂S₇ are comparable with those observed in Co₁₂P₇ and the Fe₂S polymorphs (Zurkowski *et al.*, 2022) (Fig. S-3). It was previously thought that Fe, Ni, and Co would not occupy this structure as it is composed of a majority 5-fold coordinated sites (Dharhi 1996), but this work and the synthesis of Co₁₂P₇ (Zurkowski *et al.*, 2022) proves that this structure stabilises in the Co-P and Fe-S systems with sufficient pressure and temperature.

Supplementary Tables

Table S-1 Experimental conditions and instrument parameters used for the diffraction data collected in this study. Values in parentheses are propagated uncertainties on the last reported digits.

	Run 1	Run 2
Starting composition (at. %)	Fe ₆₆ S ₃₄	
Pressure (GPa)	105.3 (9)	125 (1)
Synthesis Temperature (K)	2400 (120)	2260 (140)
Synthesis Beamline	13IDD @ APS	
Collection Temperature (K)	296	
Collection Station	13IDD @ APS	
Radiation type	synchrotron	
λ (Å)	0.2952	
Beam size (FWHM) horizontal × vertical (µm)	2 × 3	
Detector	CdTe 1M Pilatus	
Omega range (°), step size (°), exposure time (s)	±30, 0.5, 2	

Table S-2 Experimental, reduction and refinement parameters for each grain analysed in this study. Values in parentheses are propagated uncertainties on the last reported digits.

Phase Sample Name	Co ₁₂ P ₇ -type Fe ₁₂ S ₇		C22 Fe ₂ S		
	C133 P1 map 26	C133 P2 map 26	C133 P1 map 33	C133 P1 map 26	C133 P2 map 37
Synthesis					
Run #	1	2	1	1	2
Pressure (GPa)	105.3 (9)	125 (1)	105.3 (9)	105.3 (9)	125 (1)
Synthesis Temperature (K)	2400 (120)	2260 (140)	2400 (120)	2400 (120)	2260 (140)
Symmetry	Hexagonal, <i>P</i> -6, <i>Z</i> = 1		Hexagonal, <i>P</i> -62 <i>m</i> , <i>Z</i> = 3		
<i>a</i> (Å)	7.794 (2)	7.706 (3)	5.340 (3)	5.326 (7)	5.282 (5)
<i>b</i> (Å)					
<i>c</i> (Å)	3.1234 (8)	3.103 (1)	3.133 (2)	3.125 (3)	3.062 (4)
<i>V</i> (Å ³)	164.33 (8)	159.6 (1)	77.38 (9)	76.8 (2)	74.0 (2)
Reduction					
No. of measured, independent, and observed [<i>I</i> > 2σ(<i>I</i>)] reflections	386, 263, 226	357, 285, 229	142, 83, 79	135, 80, 69	128, 72, 71
<i>R</i> _{int} , <i>R</i> _{sigma}	0.014, 0.014	0.011, 0.0210	0.031, 0.017	0.058, 0.456	0.014, 0.015
Refinement					
<i>R</i> [<i>F</i> ² > 2σ(<i>F</i> ²)], <i>wR</i> (<i>F</i> ²), <i>S</i>	0.048, 0.148, 1.16	0.039, 0.109, 1.05	0.041, 0.092, 1.33	0.056, 0.128, 1.11	0.059, 0.160, 1.30
No. of reflections	263	285	83	80	72
No. of parameters	32	32	11	11	11
Δρ _{max} , Δρ _{min} (e Å ⁻³)	2.60, -1.70	2.26, -1.64	1.15, -1.19	1.31, -1.89	2.17, -2.25
Error on site occupancies	6 %	6 %	2 %	7 %	3 %

Table S-2 continued.

Phase Sample Name	C23 Fe ₂ S			Cr ₂ P-type Fe ₂ S	
	C133 P1 map 33	C133 P2 map 26	C133 P2 map 38	C133 P2 map 36	C133 P2 map 37
Synthesis					
Run #	1	2	2	2	2
Pressure (GPa)	105.3 (9)	125 (1)	125 (1)	125 (1)	125 (1)
Synthesis Temperature (K)	2400 (120)	2260 (140)	2260 (140)	2260 (140)	2260 (140)
Symmetry	Orthorhombic, <i>Pnma</i> , Z = 4			Orthorhombic, <i>Imm2</i> , Z = 12	
<i>a</i> (Å)	5.08 (1)	4.995 (4)	5.006 (3)	6.103 (4)	6.08 (1)
<i>b</i> (Å)	3.290 (2)	3.277 (2)	3.253 (2)	9.098 (4)	9.08 (1)
<i>c</i> (Å)	6.146 (8)	6.095 (2)	6.100 (7)	5.382 (1)	5.380 (3)
<i>V</i> (Å ³)	102.7 (3)	99.8 (1)	99.3 (1)	298.8 (2)	296.9 (7)
Reduction					
No. of measured, independent, and observed [<i>I</i> > 2σ(<i>I</i>)] reflections	191, 110, 88	221, 123, 106	214, 110, 101	304, 259, 218	251, 217, 191
<i>R</i> _{int} , <i>R</i> _{sigma}	0.026, 0.033	0.019, 0.0213	0.0186, 0.0178	0.037, 0.039	0.024, 0.031
Refinement					
<i>R</i> [<i>F</i> ² > 2σ(<i>F</i> ²)], <i>wR</i> (<i>F</i> ²), <i>S</i>	0.062, 0.166, 1.05	0.048, 0.123, 1.04	0.038, 0.102, 1.175	0.077, 0.193, 1.131	0.057, 0.148, 1.066
No. of reflections	110	123	119	259	217
No. of parameters	10	10	19	26	26
Δρ _{max} , Δρ _{min} (e Å ⁻³)	2.83, -2.20	1.82, -2.03	1.37, -1.66	2.40, -2.88	2.18, -2.12
Error on site occupancies	5 %	8 %	3 %	13 %	18.0 %



Supplementary Figures

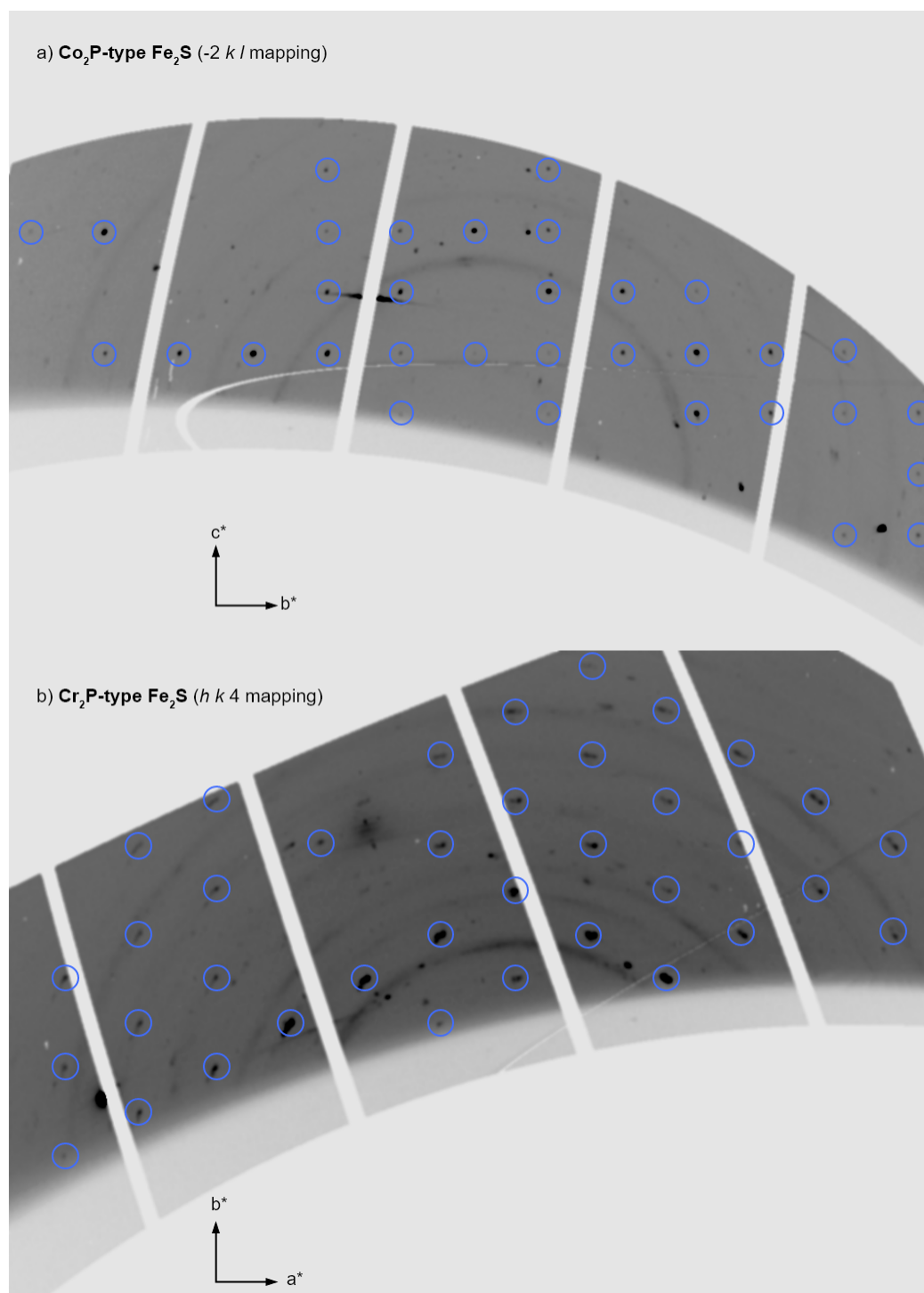


Figure S-1 Diffraction mappings of the lower-temperature (a) Co_2P -type and (b) Cr_2P -type Fe_2S polymorphs identified upon quenching from 125 GPa and 2300 K.

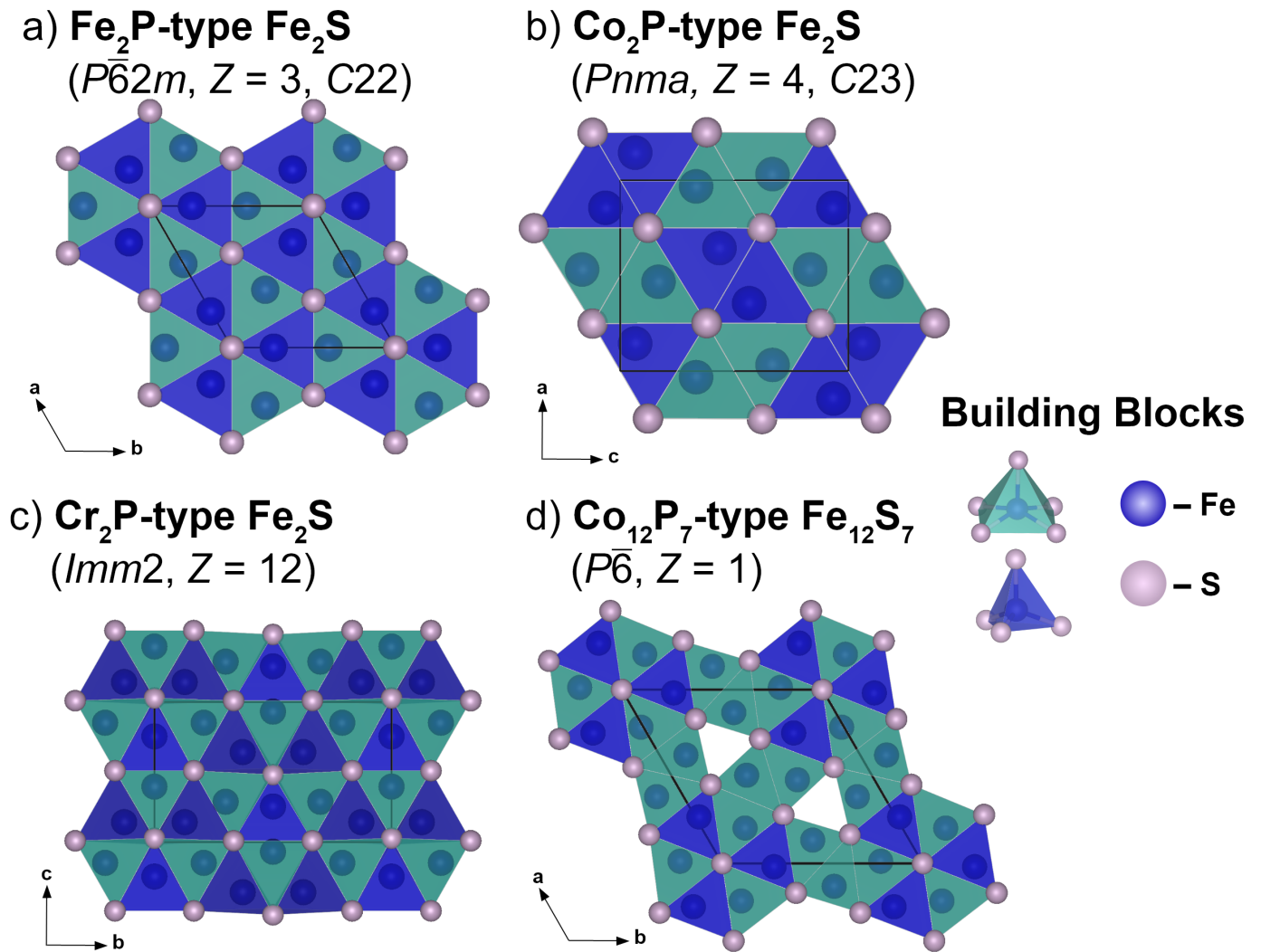


Figure S-2 Fe₂S and Fe₁₂S₇ crystal structures characterised in this study.

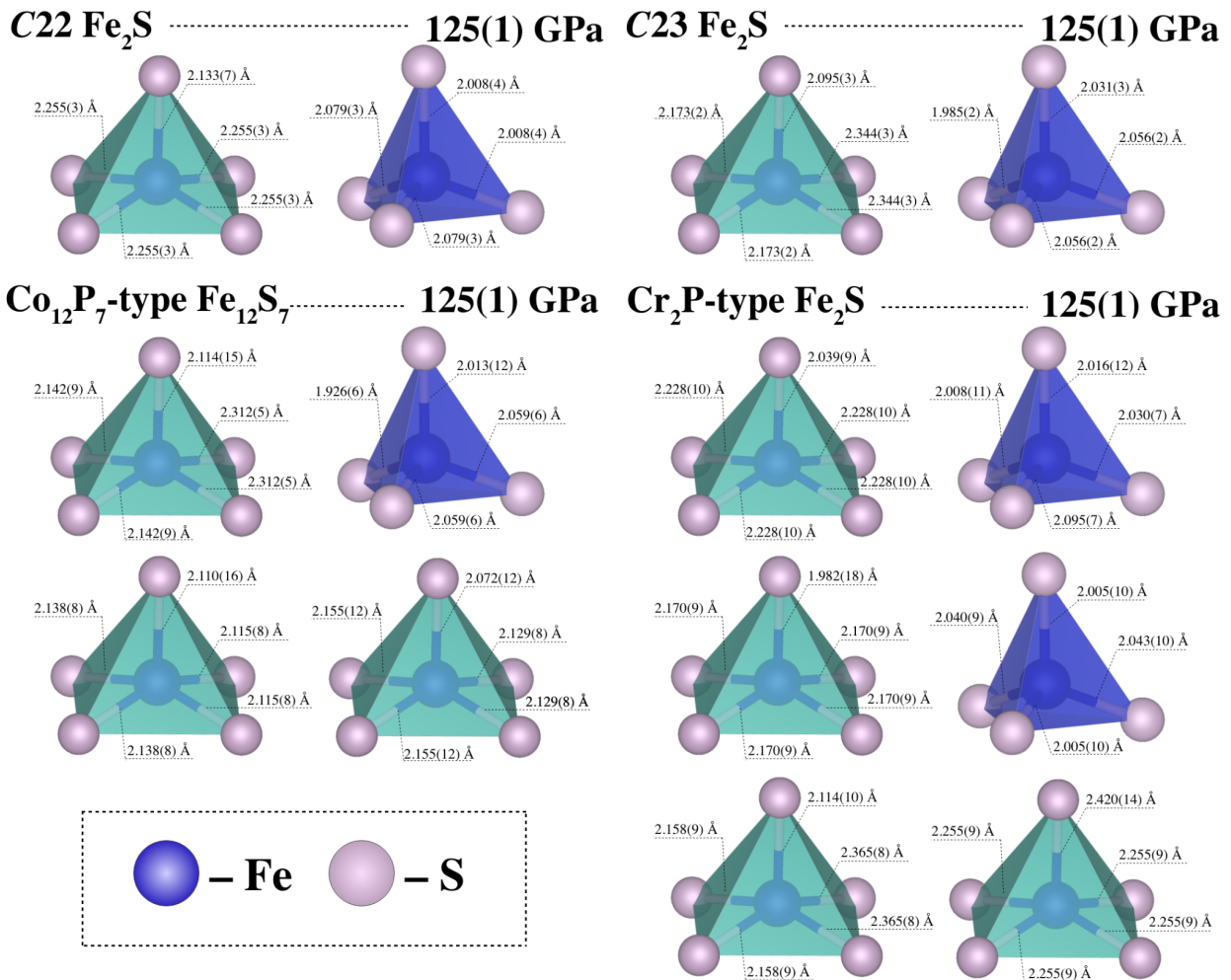


Figure S-3 Coordination polyhedra with labelled interatomic distances for C22 Fe₂S, C23 Fe₂S, Cr₂P-type Fe₂S, and Co₁₂P₇-type Fe₁₂S₇ measured at 125 GPa.

Appendices

Appendix A-1. Crystallographic information for C22 Fe₂S at 125(1) GPa.

Appendix A-2. Crystallographic information for C22 Fe₁₂S₇ at 105.3(9) GPa.

Appendix A-3. Crystallographic information for Cr₂P-type Fe₂S at 125(1) GPa.

Appendix A-4. Crystallographic information for C23 Fe₂S at 125(1) GPa.

Appendices A-1 to A-4 are Crystallographic Information Files (.cif) and can be downloaded at <https://doi.org/10.7185/geochemlet.2217>.



Supplementary Information References

- Artigas, M., Bacmann, M., Fruchart, D., Fruchart, R. (1996) La structure cristalline de Cr₂P: Distorsion orthorhombique de la structure hexagonale de type Fe₂P. *Journal of Solid State Chemistry* 123, 306–312. <https://doi.org/10.1006/jssc.1996.0184>
- Campbell, A.J., Seagle, C.T., Heinz, D.L., Shen, G., Prakapenka, V.B. (2007) Partial melting in the iron-sulfur system at high pressure: A synchrotron X-ray diffraction study. *Physics of the Earth and Planetary Interiors* 162, 119–128. <https://doi.org/10.1016/j.pepi.2007.04.001>
- Campbell, A.J., Danielson, L., Righter, K., Seagle, C.T., Wang, Y., Prakapenka, V.B. (2009) High pressure effects on the iron–iron oxide and nickel–nickel oxide oxygen fugacity buffers. *Earth and Planetary Science Letters* 286, 556–564. <https://doi.org/10.1016/j.epsl.2009.07.022>
- Chun, H.K., Carpenter, G.B. (1979) Redetermination of the Crystal Structure of Cr₁₂P₇. *Acta Crystallographica Section B: Structural Crystallography and Crystal Chemistry* 35, 30–33. <https://doi.org/10.1107/S0567740879002466>
- Dewaele, A., Belonoshko, A.B., Garbarino, G., Occelli, F., Bouvier, P., Hanfland, M., Mezouar, M. (2012) High-pressure–high-temperature equation of state of KCl and KBr. *Physical Review B* 85, 214105. <https://doi.org/10.1103/PhysRevB.85.214105>
- Dhahri, E. (1996) Etude des problèmes d'ordre et de stabilité dans les phases Ln₂M₁₂X₇ (terre rare - métal de transition - non métal). *Journal of Physics: Condensed Matter* 8, 4351. <https://doi.org/10.1088/0953-8984/8/24/004>
- Ellner, M., Mittemeijer, E.J. (2001) The Reconstructive Phase Transformation β-Co₂P → α-Co₂P and the Structure of the High-Temperature Phosphide β-Co₂P. *Zeitschrift für anorganische und allgemeine Chemie* 627, 2257–2260. [https://doi.org/10.1002/1521-3749\(200109\)627:9<2257::AID-ZAAC2257>3.0.CO;2-W](https://doi.org/10.1002/1521-3749(200109)627:9<2257::AID-ZAAC2257>3.0.CO;2-W)
- Heinz, D.L., Jeanloz, R. (1987) Measurement of the melting curve of Mg_{0.9}Fe_{0.1}SiO₃ at lower mantle conditions and its geophysical implications. *Journal of Geophysical Research: Solid Earth* 92, 11437–11444. <https://doi.org/10.1029/JB092iB11p11437>
- Lavina, B., Dera, P., Downs, R.T. (2014) Modern X-ray diffraction methods in mineralogy and geosciences. *Reviews in Mineralogy and Geochemistry* 78, 1–31. <https://doi.org/10.2138/rmg.2014.78.1>
- Prakapenka, V.B., Kubo, A., Kuznetsov, A., Laskin, A., Shkurikhin, O., Dera, P., Rivers, M.L., Sutton, S.R. (2008) Advanced flat top laser heating system for high pressure research at GSECARS: application to the melting behavior of germanium. *High Pressure Research* 28, 225–235. <https://doi.org/10.1080/08957950802050718>
- Prescher, C., Prakapenka, V.B. (2015) *DIOPTAS*: a program for reduction of two-dimensional X-ray diffraction and data exploration. *High Pressure Research* 35, 223–230. <https://doi.org/10.1080/08957959.2015.1059835>
- Rigaku Oxford Diffraction* (2018) CrysAlisPRO software system, v. 1.171.39.44a. Rigaku Corporation, Oxford, U.K.
- Sheldrick, G.M. (2014) *SHELXL-2014/7: Program for the Solution of Crystal Structures*. University of Göttingen, Göttingen, Germany.
- Sheldrick, G.M. (2015a) *SHELXT* - Integrated space-group and crystal-structure determination. *Acta Crystallographica Section A: Foundations and Advances* 71, 3–8. <https://doi.org/10.1107/S2053273314026370>
- Sheldrick, G.M. (2015b) Crystal structure refinement with *SHELXL*. *Acta Crystallographica Section C: Structural Chemistry* 71, 3–8. <https://doi.org/10.1107/S2053229614024218>
- Zurkowski C.C., Lavina B., Chariton S., Greenberg E., Prakapenka V.B., Campbell A.J. (2022) The crystal structure of Fe₂S at 90 GPa based on single-crystal X-ray diffraction techniques. *American Mineralogist* 107, 739–743. <https://doi.org/10.2138/am-2022-7973>

